Materials Science & Engineering A 820 (2021) 141561

Contents lists available at ScienceDirect

Materials Science & Engineering A

journal homepage: www.elsevier.com/locate/msea

The formation mechanism, growth, and effect on the mechanical properties of precipitate free zones in the alumina-forming austenitic stainless steel Fe–20Cr–30Ni–2Nb–5Al during creep

Andrew Peterson *, Ian Baker

Thayer School of Engineering, Dartmouth College, 14 Engineering Drive, 03755, Hanover, NH, United States

ARTICLE INFO

Keywords:
AFA steel
Precipitate free zone
Grain boundary
Creep

ABSTRACT

The mechanisms of formation and growth of $L1_2$ precipitate-free zones (PFZs) in the alumina-forming austenitic stainless steel Fe–20Cr–30Ni–2Nb–5Al during creep were studied using scanning electron microscopy and energy dispersive x-ray spectroscopy. The PFZs formed following the dissolution of $L1_2$ precipitates due to depletion of nickel and aluminum. Little PFZ growth occurred until the grain boundaries were substantially covered by Laves phase and B2 precipitates large enough to deplete the surrounding grain of nickel and aluminum. This resulted in the dissolution of the $L1_2$ precipitates. Additionally, micro-cracks observed in the PFZ at long creep times suggest that the PFZ is ultimately the weakest point in the microstructure, and that fracture initiates there.

1. Introduction

Alumina-forming austenitic stainless steels (AFAs) are a new class of steels being designed for high temperature applications. One particular area of interest is in steam powerplants, where operating at higher temperatures results in higher efficiency and fewer harmful emissions [1–3]. AFAs show great promise for these high temperature applications in harmful environments because: 1) they display excellent corrosion resistance, particularly in water vapor/steam containing environments, due to formation of a protective alumina layer [4–9]; 2) they show promising high temperature strength results when compared to both advanced austenitic stainless steels and some Ni-base superalloys [5,6,10]; and 3) they are more affordable than other options, like Ni-base superalloys, due to their lower Ni content. However, further understanding of the microstructure and how it affects high temperature strength is needed to optimize the mechanical properties for high temperature use.

AFAs have complicated microstructures, which generally have several types of precipitates both in the matrix and along the grain boundaries (GBs). This study focuses on the alloy Fe–20Cr–30Ni–2Nb–5Al, which contains Laves phase Fe_2Nb precipitates both in the matrix and on the GBs, B2 (ordered b. c.c.)-structured NiAl precipitates both in the matrix and on the GBs, and $L1_2$ (ordered f. c.c.)-structured Ni_3Al precipitates in the matrix during creep at 750 °C. Additionally, there is a $L1_2$ precipitate free zone (PFZ) along the GBs. Research has produced a good understanding of the evolution of these precipitates in this alloy during creep at 750 °C, and how the size, spacing, and location of each precipitate type affects the creep strength [11]. Briefly, of various anneals tried, a 2.4 h anneal at 800 °C produces the best high temperature strength [12]. After this anneal, there are small (~100 nm) Laves phase and B2 precipitates both in the matrix and on the GBs but no $L1_2$ precipitates are present. Nano-sized $L1_2$ matrix precipitates nucleate in the matrix during creep and increase in volume fraction and coarsen, following the Ostwald ripening law during creep [11]. The Laves phase and B2 precipitates in the matrix also increase in volume fraction and coarsen following the Ostwald ripening law during creep. Additionally, the GB percent coverage by Laves phase and B2 precipitates increases throughout creep. The $L1_2$ precipitates are the dominant strengthening mechanism in the matrix due to their small interparticle spacing. It is commonly reported in the literature that nano-sized $L1_2$ precipitates or carbides provide significant strengthening in other AFA alloys at elevated temperatures [4,6,10,13–15]. Additionally, the Laves phase and B2 precipitates covering the GBs strengthen the alloy. However, the alloy ultimately fails intergranularly, indicating either that the GB precipitates or PFZ are the weak point in the microstructure [11,16]. A GB strengthening mechanism has been reported in other AFA alloys [17] as well as intergranular fracture along coarse GB precipitates [18]. However, there is not a good understanding

* Corresponding author.
E-mail address: andrew.c.peterson.th@dartmouth.edu (A. Peterson).

https://doi.org/10.1016/j.msea.2021.141561
Received 9 April 2021; Received in revised form 21 May 2021; Accepted 2 June 2021
Available online 11 June 2021

of the formation mechanism, growth, and the effect on the mechanical properties of the PFZ.

While the formation of a PFZ was initially proposed to be the result of and proof of the occurrence of diffusion creep [19,20], this has since been disproved [21,22] and there are three currently accepted mechanisms for the formation of the PFZ. First, the PFZ forms as a result of the dissolution of precipitates due to GBs sliding and migration during creep [21]. Second, the PFZ forms due to the depletion of vacancies near the GB. The GB is a vacancy sink, creating an area around the GB with a lower density of vacancies. Vacancies are sites for heterogenous nucleation, and a lack of vacancies prevents precipitate nucleation. Even if the solute concentration is sufficient for stable precipitates to form, they will not have the nucleation sites needed, thus, resulting in the formation of the PFZ. This has been reported as the mechanism of PFZ formation in several alloys [23–26]. Third, the PFZ forms due to a depletion of particular elements near the GB. The GB itself is a heterogeneous nucleation site and this means that precipitates are likely to nucleate there first. Solute will be removed from the surrounding area and the matrix becomes solute-depleted in an area around the GB. This process can also lead to the PFZ and has been reported in numerous alloys [18, 27–32]. Maldonado and Nembach [28] split this process into two separate mechanisms: direct and indirect. In direct solute loss, the elements from which the precipitates form diffuses to the GB precipitates. For example, Maldonado and Nembach noted that in a Ni-base superalloy in which Ti-containing carbides precipitate on the GB, as the Ti diffuses to the GB the γ' (Ni_3Ti) precipitates in the matrix dissolve, and a PFZ forms. A similar mechanism has been reported in an Al–Li alloy [32]. In indirect solute loss, an element diffuses to the GB precipitates, which then affects the solubility of another element. For example, Cr loss to carbides along the GB has been reported in Ni-base alloys, resulting in lower solubility of Ti and a resulting γ' (Ni_3Ti) PFZ [33,34]. However, there is some dispute about its occurrence since researchers have suggested that Cr does not decrease the solubility of the γ' formers and that Ti-rich carbides are the cause of the solute depletion in Ni-base alloys [28]. Researchers have even reported the PFZ formation being caused by both vacancy depletion and solute depletion near the GBs, with the vacancy depletion driving the initial formation of the PFZ, followed by a stage where the PFZ disappears, and then solute depletion propels the formation of the PFZ at long anneal times [35].

Several researchers have developed equations that approximate the growth of the PFZ due to diffusion of atoms that rely on a square-root dependence with time [18,28,30,32]. These have been corroborated with experimental findings showing that the PFZ width has a linear relationship with the square-root of time [18,28,30,32,36]. In some cases, the PFZ initially grows with a $t^{1/2}$ relationship before reaching a limit beyond which the width no longer increases [28].

In precipitation-hardened materials, it is reasonable to assume that the alloy will be softer in the PFZ than in the rest of the grain. Nanoindentation tests have been performed on several alloys in both the PFZ and the surrounding grain to determine the difference in hardness. In AlZnMg and AlZnMgAg alloys containing a PFZ it was found that three different regions existed: the PFZ, which was the softest region; the transition region, where the hardness begins to increase; and the grain interior, where the hardness reaches its maximum and steady-state value [37]. This transition region was attributed to less effective solid-solution strengthening than in the PFZ and less effective precipitation-hardening than in the matrix due to a lower density of precipitates. In an AlCuSiGe alloy with a PFZ, the hardness was similarly found to have the same three regions [38]. Nanoindentation tests have not yet been performed in the PFZ on γ'-strengthened alloys. However, a series of tensile test experiments along with *in-situ* TEM straining have been performed on a Ni-base superalloy [27,39,40]. These results found that a PFZ larger than 1.7 × (interparticle spacing – average particle radius) led to a decrease in the yield strength by up to 25%. *In-situ* TEM straining revealed that the PFZ was softer than the surrounding matrix due to the ease with which dislocations were generated in the PFZ.

A recent study of a different AFA alloy found that the growth of the PFZ appeared to follow a $t^{1/2}$ relationship. It was suggested that this meant the PFZ width was controlled by diffusion of Al to the B2 precipitates on the GB [18]. However, the PFZ was only measured at three creep times – making it difficult to confirm the $t^{1/2}$ relationship. Additionally, no compositional data was gathered across the GB/PFZ to confirm the suggested depletion of Al. Earlier work has shown that AFA alloys tend to fracture intergranularly during creep [11,18], indicating that either the coarse GB precipitates or the PFZ are the weakest point of the microstructure. In this paper we present a microstructural examination of crept of the AFA steel Fe–20Cr–30Ni–2Nb–5Al in order to understand the formation mechanism and growth behavior of the PFZ in AFA alloys and its effect on the mechanical properties.

2. Experimental

Fe–20Cr–30Ni–2Nb–5Al (at. %) was cast into an 8 kg ingot using split-cast vacuum induction by Carpenter Technology Corporation. The ingot was press-forged into 19 mm × 19 mm x 600 mm rectangular bars. A solutionizing anneal was then performed in an argon atmosphere for 24 h at 1250 °C, resulting in a grain size of ~450 μm. The samples were then annealed in air at 800 °C for 2.4 h and quickly cooled in air. Creep tests were then performed, as discussed in detail in previous work, on dog-bone shaped tensile creep specimens [11,16]. Creep tests analyzed in this study were performed at 750 °C and 45 MPa for 250, 500, 1000, 1500, 2000, and 4000 h, as well as at 730 °C and 770 °C at 45 MPa for 2000 h. Note that the creep test temperature was initially reported as the nominal temperature [11], but measurement with an external thermocouple showed the dog-bones were approximately 10 °C less than the nominal temperature. The temperature measured with the external thermoucouple is reported here. All creep tests analyzed in this study were terminated prior to failure. The creep tests were performed on home-built, constant stress creep jigs, based on a design by Garofolo, Richmond, and Domis [41].

3 mm diameter cylindrical microscopy samples were cut from the crept dog-bones using electro-discharge machining. The cylinders were sliced into thin discs and polished with silicon carbide paper to ~100 μm thick. The discs were electro-polished using a Struers TenuPol in an electrolyte of 20% nitric acid in methanol at −40 °C to −20 °C, 11 V, ~100 mA, and a flow rate of 15, followed by rinsing alternately in ethanol and methanol three times. Scanning electron microscope (SEM) imaging was performed on a FEI (Thermo Fisher Scientific) Helios 5CX dual beam field emission gun (FEG) SEM. The backscattered electron (BSE) detector was used to distinguish between precipitates, with the Laves phase precipitates appearing light and the B2 phase precipitates appearing dark [42]. For images which required higher magnification, secondary electron (SE) imaging was used because a smaller working distance could be used yielding higher resolution of nano-sized precipitates. ImageJ was used to perform PFZ measurements. Ten images were analyzed for each condition, and ten measurements were taken from each image for a total of one hundred data points for each measurement at each condition. 95% confidence intervals were then calculated for error bars. Energy dispersive X-ray spectroscopy (EDS) was performed using the Oxford Instruments UltimMax 100 X-ray detector and electron backscatter diffraction (EBSD) was performed using an Oxford Instruments Symmetry EBSD detector.

3. Results

3.1. Creep tests

Creep curves for each temperature tested are shown in Fig. 1. Note the obvious increasing secondary creep rate with increased temperature. At 730 °C and 770 °C, only single tests were performed. At 750 °C, tests were performed for various lengths to analyze the microstructure after different creep times. All tests were stopped prior to failure.

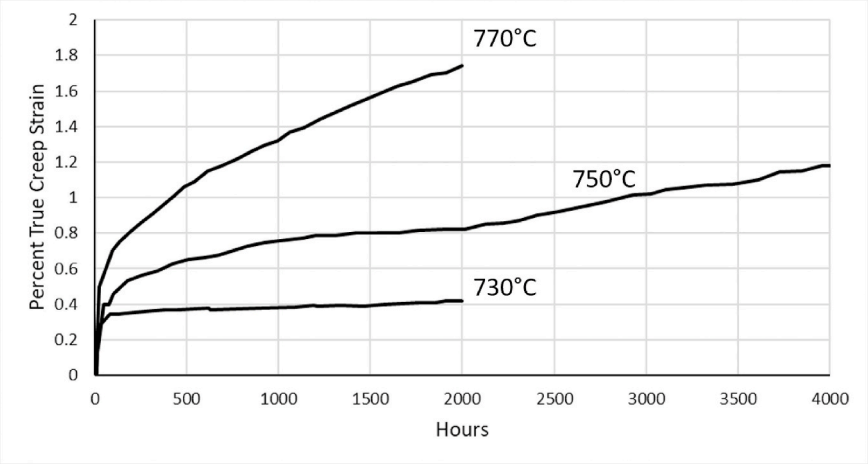

Fig. 1. Strain versus time for Fe–20Cr–30Ni–2Nb–5Al at 45 MPa and the temperatures indicated. Note that multiple tests were performed at 750 °C and only the longest duration test is shown here.

3.2. SEM imaging and PFZ/GB width measurements

SEM imaging was performed after each creep test to measure the width of the $L1_2$ PFZ and the size of the GB precipitates. This was performed for both the gauge of the dog-bone, i.e. applied stress was present, and for the head of the dog-bone, i.e. no stress was applied. Fig. 2 shows examples of each kind of precipitate in the alloy and examples of each measurement made. The $L1_2$ precipitates appear as small white dots, the Laves phase precipitates are the larger plate-like precipitates that also are light, while the B2 precipitates the dark plate-like precipitates. The measurement *w'* represent the width of the PFZ from the edge of the GB precipitates (or the GB itself, if no GB precipitate was present) to the edge of the PFZ. The measurement *w* represents the width of the PFZ from the GB to the edge of the PFZ. However, the GB is often covered by precipitates which makes it difficult to determine where exactly the GB is. Thus, this was measured as 2w by measuring completely across the PFZ. Finally, the measurement *GB_w* = 2*w*-2*w'* represents the width of the GB precipitates.

In addition to the Laves phase, B2, and $L1_2$ precipiates, further analysis of the crept specimens revealed a fourth precipitate – a FeCr Sigma phase. The Sigma phase is difficult to detect because it exhibits very similar contrast to the matrix in the SEM images, see Fig. 3. The Sigma phase was present at all temperatures, primarily after long creep times, i.e. 2000 h or longer. It made up a much smaller fraction than any of the other precipitates, and was generally present along the GBs.

Imaging was performed after each creep time to monitor the width of the PFZ and the GB precipitates. Fig. 4 shows representative SEM images of the GB/PFZ when the GB is covered by precipitates for various creep times at 750 °C. Fig. 4a shows the GB/PFZ after 250 h. The PFZ is very small and is present in some areas but not others. Fig. 4b shows the GB/PFZ after 1000 h, here the PFZ has increased in size and covers almost the entirety of the GB. Fig. 4c and d shows the GB/PFZ after 2000 h and 4000 h, respectively. It is clear at these long creep times that the PFZ width has increased significantly and that the PFZ covers the entirety of the GB. While discussion of the PFZ up to this point has focused on the PFZ around the GBs, it is also interesting to note that a PFZ forms around large matrix precipitates – which is clearly visible in these images from long creep times. This will be discussed more later.

While the previous images showed GBs covered by precipitates, it is important to remember that at short creep times much of the GB was not

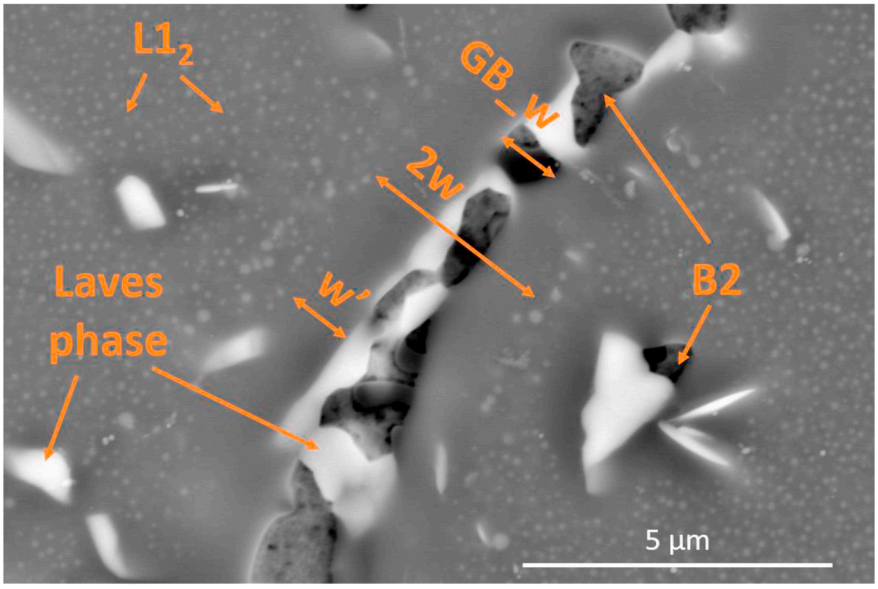

Fig. 2. BSE image showing examples of precipitates in Fe–20Cr–30Ni–2Nb–5Al after creep for 4000 h at a load of 45 MPa at 750 °C. The sample was taken from the head of the creep dog-bone, and thus no stress was applied. Examples of PFZ and GB measurements are noted.

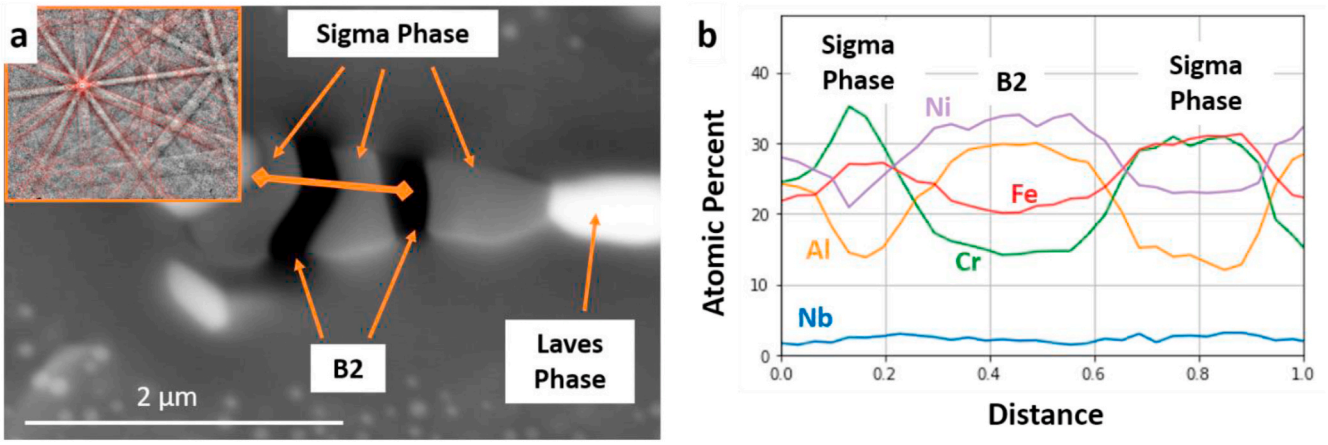

Fig. 3. Fe–20Cr–30Ni–2Nb–5Al after creep at 750 °C and 45 MPa for 2000 h. a) BSE image of GB showing examples of Laves phase, Sigma phase, and B2 precipitates. EBSD pattern of Sigma phase is inset. b) EDS line scan across the area in (a) marked with a solid line. The Sigma phase and B2 precipitates are identified on the line scan.

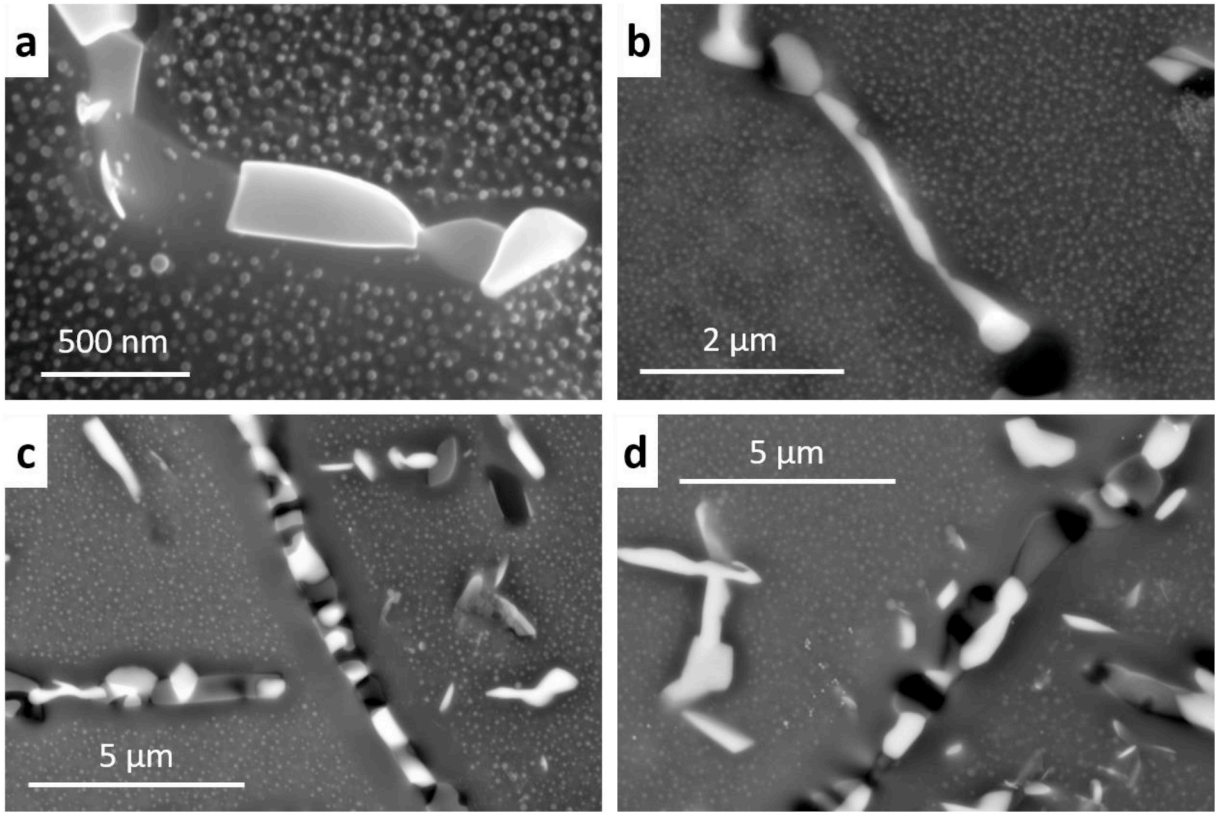

Fig. 4. SEM images of Fe–20Cr–30Ni–2Nb–5Al, a) SE image of the dog-bone head after 250 h at 750 °C, b) BSE image of the dog-bone head after 1000 h at 750 °C, c) BSE image of the dog-bone head after 2000 h at 750 °C, and d) BSE image of the dog-bone head after 4000 h at 750 °C. See text for details.

covered by precipitates. Fig. 5 shows representative images of the GB/PFZ when no GB precipitates are present after various creep times. Fig. 5a shows a very small PFZ present after 250 h of creep. However, as noted previously, not all sections of the GB had a PFZ at these short creep times, see Fig. 5b. Fig. 5c shows an image after 1000 h of creep, in which a PFZ is present along nearly the entire length of the GB – even with no precipitate present. Finally, Fig. 5d shows an image after 4000 h of creep, in which there are only small sections of the GB which are not covered by precipitates – and it can clearly be seen that a wide PFZ is present along the entire length of the GB.

Fig. 6 shows values of both *w'* and *w* as a function of time. Both measurements show similar trends. First, there is little difference between the measured widths in the head and the gauge of the dog-bone. For all creep times, the measured values are well within the 95% confidence intervals. Second, there is little growth of the PFZ for creep times up to ~500 h. After this, the growth rate increased significantly up to 2000 h. Between 2000 h and 4000 h the growth rate decreased. Third, the PFZ width has a large dependence on temperature, as indicated by the tests performed for 2000 h at different temperatures.

Fig. 7 shows measured *GB_w* versus creep time as well as the percent GB area coverage by precipitates versus time. Note that GB coverage was also measured and reported in a previous study of these creep tests [11].

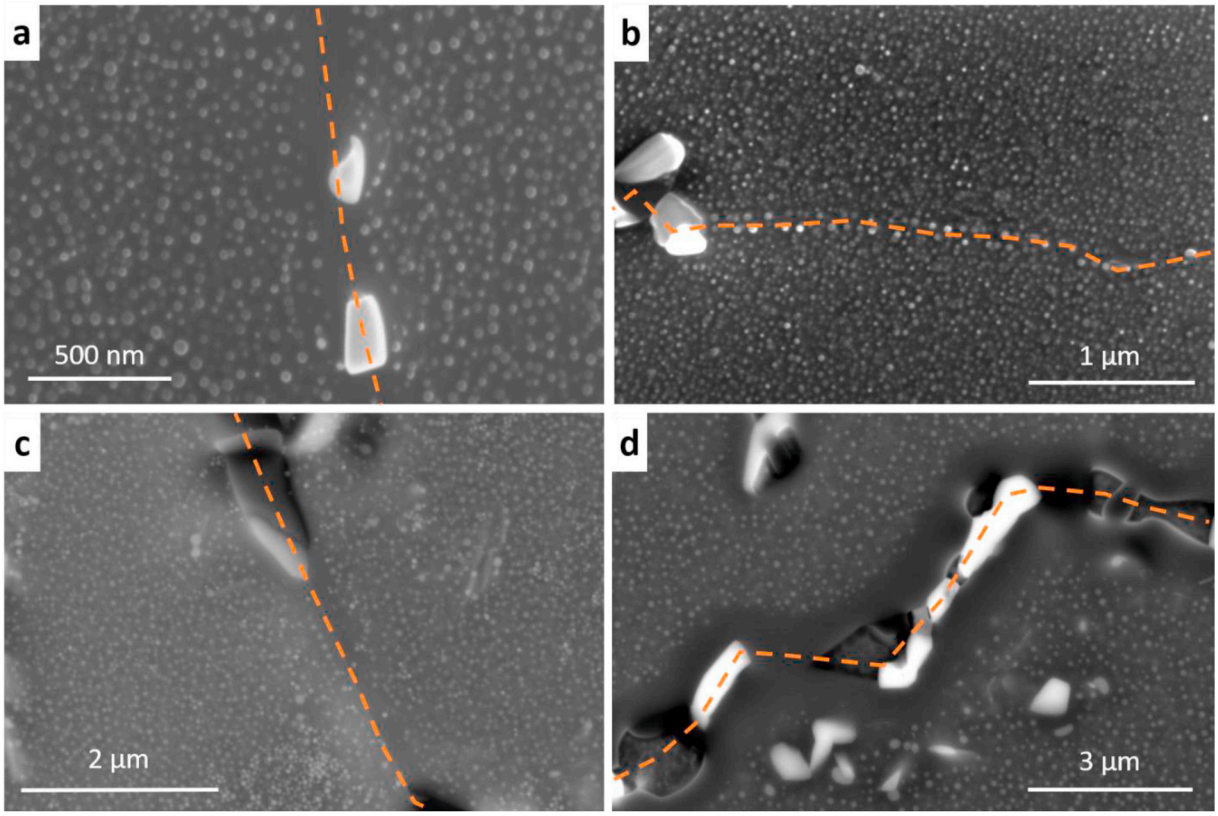

Fig. 5. SEM images of Fe–20Cr–30Ni–2Nb–5Al after, a) SE image of the dog-bone gauge after 250 h at 750 °C, b) SE image of the dog-bone gauge after 500 h at 750 °C, c) BSE image of the dog-bone gauge after 1000 h at 750 °C, and d) BSE image of the dog-bone gauge after 4000 h at 750 °C. The dashed line represents the GBs. See text for details.

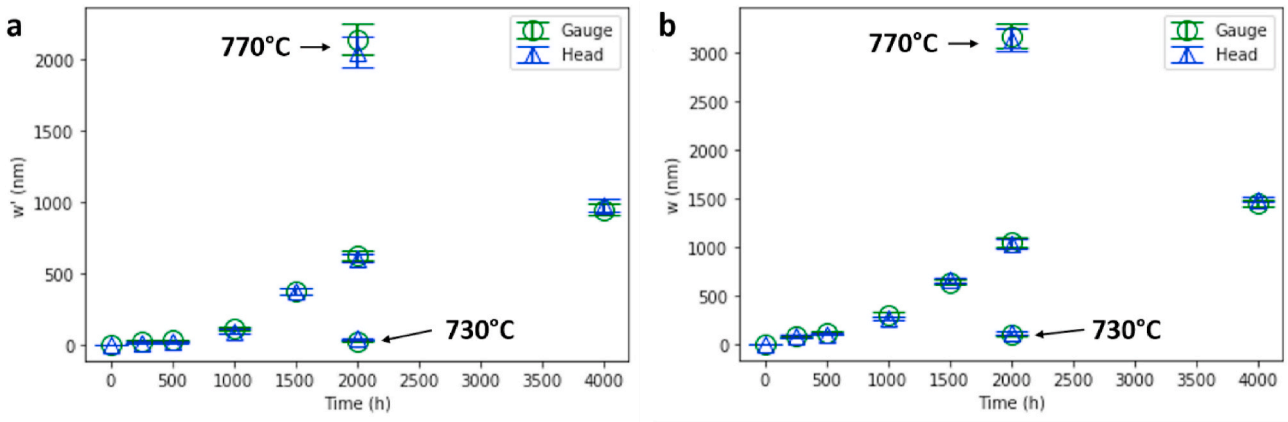

Fig. 6. PFZ width versus time for Fe–20Cr-30 Ni–2Nb–5Al during creep. a) PFZ width w' versus time, and b) PFZ width w versus time. All tests were performed at 750 °C unless otherwise noted. Error bars represent 95% confidence intervals. Note there is little difference in the width for specimens taken from the gauge and from the head of the specimen.

The values reported here are slightly higher because higher magnification images were used for the measurements. This means that very thin GB precipitates were measured, which likely were not able to be measured previously. Also, the Sigma phase has now been identified and incorporated into the measurements which leads to a slight increase in GB coverage. However, it should be noted that the values from both measurements are within the 95% confidence intervals for each creep time. Similar to the PFZ width measurements, the GB width shows no significant difference between values for the head versus the gauge of the dog-bone. The growth of the GB width appears to follow an approximately linear relationship with time for the first 2000 h, and then shows only slight growth from 2000 h to 4000 h. The GB area percent coverage at 750 °C shows that initially the GB coverage with precipitates was quite small, with less than 50% of the GB covered with precipitates prior to creep. After 500 h of creep this increased to ~60% coverage, and then further increased to ~90% coverage by 4000 h of creep.

In summary, at creep times of 500 h or less, the PFZ was very small (~average *w'* of 30 nm or smaller) and was only present along some portions of the GB. At creep times of 1000 h or longer, a PFZ was present along nearly the entire length of the GB and grew significantly faster. Additionally, the GB precipitate width increased with creep time –

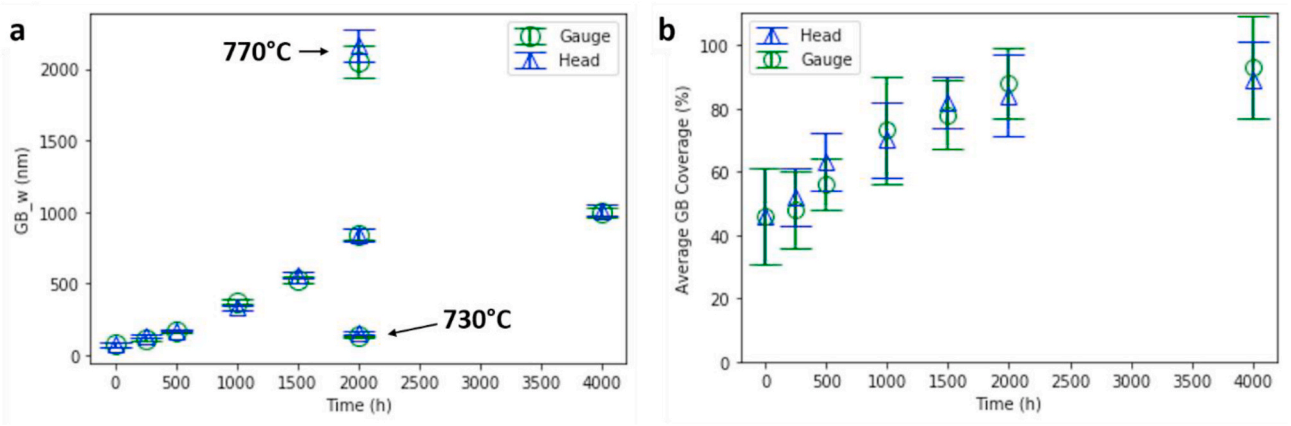

Fig. 7. a) GB_w versus time for Fe–20Cr–30Ni–2Nb–5Al during creep. All tests were performed at 750 °C unless otherwise noted. b) percent GB coverage versus time for Fe–20Cr–30Ni–2Nb–5Al during creep at 750 °C. For both plots the error bars represent 95% confidence intervals.

showing a linear growth rate up to 2000 h, before showing decreased growth between 2000 h and 4000 h. All PFZ width and GB width measurements showed a strong dependence on temperature. It should also be noted that GB coverage increased throughout creep time.

Not only did a PFZ form around the GBs, but as noted before, a PFZ formed around Laves phase and B2 precipitates in the matrix. Fig. 8a shows a small PFZ around a Laves phase precipitate after 250 h, and Fig. 8b shows a larger PFZ around Laves phase and B2 precipitates after 4000 h.

A study on another AFA alloy reported substantial cracking along the entirety of the GBs after creep failure [43]. While previous research on this alloy reported that no similar large cracking was observed in the PFZ after the tests studied here [11], further analysis of the GBs and PFZ revealed evidence of micro-cracks in the PFZ but only for the creep test performed at 750 °C and 45 MPa which was terminated after 4000 h. This is shown in Fig. 8, where micro-cracks are observed in a specimen from the 4000 h creep test – the longest test analyzed in this study. Such micro-cracks were only seen in a very small fraction of SEM images. Fig. 9.

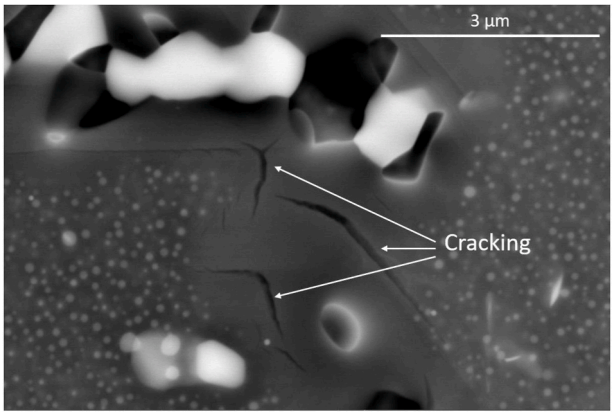

Fig. 9. BSE image showing evidence of micro-cracks forming in the PFZ along a GB of Fe-20-Cr-30Ni–2Nb–5Al after creep for 4000 h at 750 °C and 45 MPa. Note that the test was terminated and did not fail.

3.3. EDS line scans

SEM EDS line scans were performed across both the PFZ and GBs to determine if there was any change in chemistry in the PFZ and surrounding grain. It should be noted that due to spatial resolution limitations, these results show general trends in composition but lack the resolution to clearly define the compositional gradient at the precipitate interfaces. Fig. 10 shows representative line scans of the PFZ around GB precipitates after creep for 4000 h at 750 °C. Fig. 10a shows a line scan across a Laves phase precipitate on a GB, as well as the surrounding PFZ and grain. Fig. 10b shows a line scan across a B2 precipitate on a GB, as well as the surrounding PFZ and grain. In both cases, there is a clear depletion of Ni in the PFZ compared to the surrounding $L1_2$-containing matrix. While there also appears to be some depletion of Al in the PFZ, this was not observed in all EDS line scans and was not as pronounced as the Ni depletion. These results indicate that there is a change in local composition near the large GB precipitates.

EDS line scans were also performed across the PFZ when no GB

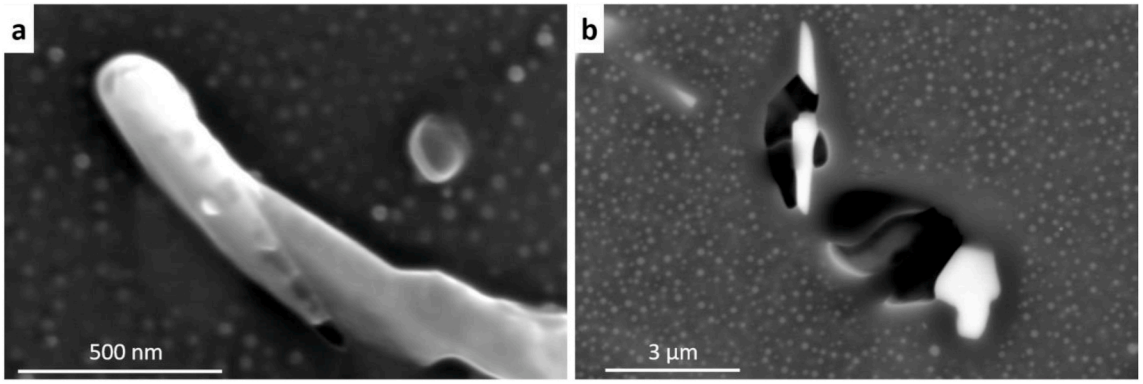

Fig. 8. PFZ around matrix precipitates in Fe–20Cr–30Ni–2Nb–5Al. a) SE image of small PFZ around Laves phase precipitate in dog-bone head after creep for 250 h. b) BSE image of PFZ around Laves phase and B2 precipitates in dog-bone head after creep for 4000 h.

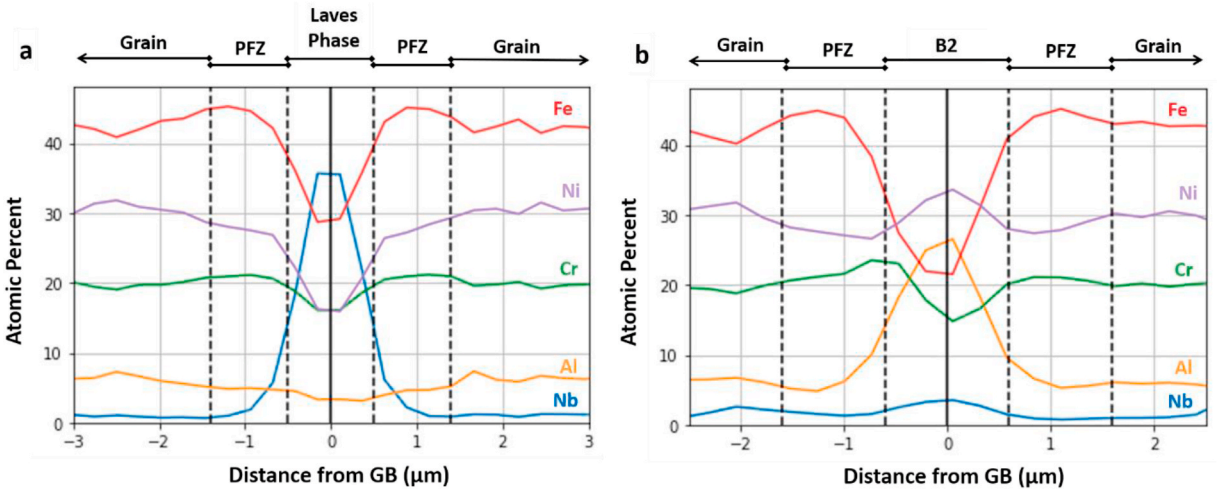

Fig. 10. EDS line scans of Fe–20Cr–30Ni–2Nb–5Al dog-bone head after 4000 h at 750 °C. a) Line scan across a Laves phase precipitate on a GB. b) Line scan across a B2 precipitate on a GB.

precipitates were present, see Fig. 11 which shows the PFZ after 1000 h. Even with no GB precipitates present, there is clearly a lower Ni concentration in the PFZ region as well as the grain region close to the PFZ. It should be noted there is also an increase in Nb near the GB. This dicates that the Nb may be segregating to the GB and causing a change in local composition.

4. Discussion

4.1. formation mechanism

The experimental results presented above can be used to determine the formation mechanism of the PFZ. To start, the mechanisms which do not fit the data can be ruled out. First, the formation of the PFZ due to GB sliding and migration can be ruled out. The PFZ existed in both the head and the gauge of the dog-bone and was of a similar size in the head and gauge for all conditions. This suggests that GB sliding and migration has little to do with PFZ formation in this alloy, since no GB sliding would occur in the head of the dog-bone where no stress was applied. Additionally, a previous study on this alloy using diamond stylus markings during creep to track GB sliding found that there was little or no GB sliding [16]. If no GB sliding occurs, then this mechanism of PFZ formation would not occur.

Second, the formation of the PFZ due to vacancy depletion can be excluded. As presented in Figs. 4 and 5, at short creep times (500 h or less) the PFZ is either extremely small or in some cases does appear to not exist. This shows that the $L1_2$ precipitates were able to nucleate but then dissolved. Additionally, it should be considered that the GB precipitate width increases significantly during creep. As the width of the GB precipitates increase, the PFZ is moved further out from the GB. Thus, at long creep times the entirety of the PFZ is now in an area which was once fully covered with $L1_2$ precipitates. Similarly, this means that the $L1_2$ precipitates were able to nucleate, but then they later dissolved. A similar situation occurs for Laves phase and B2 precipitates in the matrix. As these precipitates coarsen, the PFZ moves further out from the center of the precipitate. Again, at long creep times the entirety of

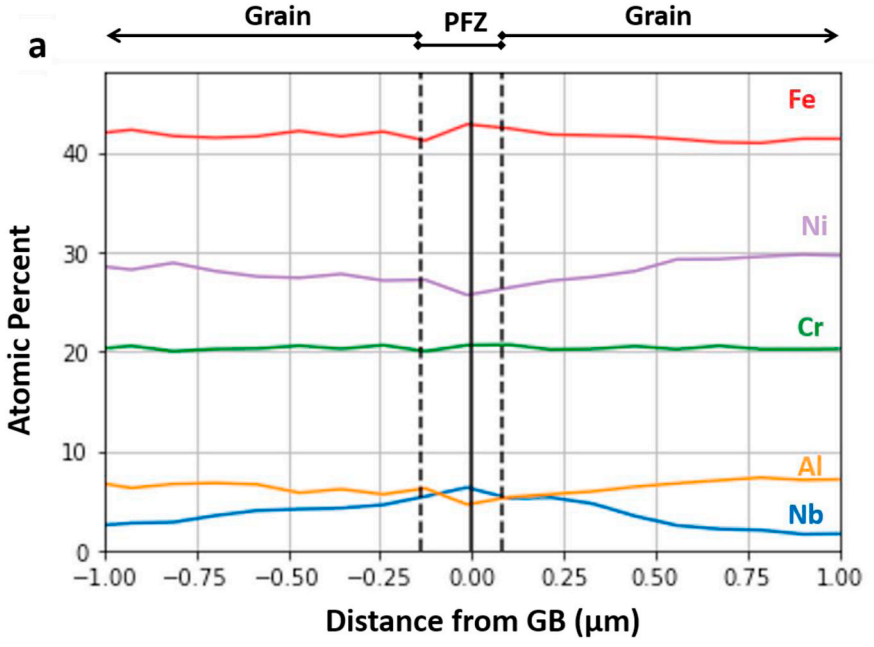

Fig. 11. EDS line scan of PFZ around GB in Fe–20Cr–30Ni–2Nb–5Al with no GB precipitate. Sample taken from dog-bone head after 1000 h at 750 °C.

the PFZ is now in an area which was once fully covered with $L1_2$ precipitates. The vacancy depletion mechanism of PFZ formation indicates that precipitates are not able to nucleate due to a lack of heterogeneous nucleate sites. The results presented here clearly show the $L1_2$ precipitates were able to nucleate, but then later dissolved.

This brings up the third possibility – PFZ formation due to solute depletion. This theory fits the presented data. EDS line scans show a clear depletion of Ni in the PFZ. While depletion of Al in the PFZ was observed in some cases, this was not seen in every EDS scan of the PFZ. This suggests that the depletion of Ni is the controlling factor in PFZ formation. As the $L1_2$ precipitates have a nominal composition of Ni_3Al, it is clear that a depletion of Ni and Al would lead to dissolution of the $L1_2$ precipitates. The results suggest that solute depletion may be occurring due to both direct and indirect solute loss. Near B2 NiAl precipitates, there is direct solute loss as Ni and Al are consumed by the B2 precipitates – which have been reported to be more thermodynamically stable [18]. This is occurring near B2 precipitates both in the matrix and along the GBs. As the B2 precipitates increase in size they consume more Ni and Al, which explains the increase in PFZ width with creep time. Additionally, it is possible there is indirect solute loss near the Laves phase precipitates. As there is a clear depletion of Ni near the Laves phase precipitates in the presented EDS line scan, it is likely that there is a local composition change in this region which is leading to this solute depletion. Higher resolution composition data will need to be acquired to confirm this. It is also interesting to note that there appears to be a depletion of Ni even with no GB precipitates present. This decrease in Ni was accompanied by an increase in Nb at the GB. It is possible that Nb is segregating to the GBs leading to a local composition change, resulting in a lower solubility of Ni. Nb segregation to GBs has been reported in several other alloys [44,45]. However, this likely only plays a role for short creep times (<1000 h). At long creep times the GB is almost completely covered with Laves phase and B2 precipitates, and the solute depletion likely becomes controlled by these precipitates. It was difficult to determine what effect the Sigma phase precipitates had on PFZ formation. The Sigma phase always formed on B2 precipitates. EDS line scans across the Sigma phase also picked up X-rays from B2 preciptiates, thus, it was difficult to distinguish the effect of the Sigma phase from the effect of the B2 precipitates. As the Sigma phase only covered a very small fraction of the GBs, it is likely that they had little effect on PFZ formation and growth.

4.2. growth

Several models have been proposed for the growth of the PFZ due to diffusion of atoms through the matrix [18,28,30,32]. All of these models have the form:

$$w = k\sqrt{t} \qquad \text{equation 1}$$

Where w is the PFZ width from the GB to the edge of the PFZ (as defined previously), k is a variable which is dependent on the concentration gradient in and near the PFZ, and t is time. Thus, a plot of w versus $t^{1/2}$ is shown in Fig. 12. As reported in the Results section, little growth of the PFZ was seen up to 500 h. The little PFZ growth for times up to 500 h is likely because the GB precipitates were small and did not cover a sufficient fraction of the GB for solute depletion to occur. This is a likely explanation for the limited growth up to 500 h. However, the data in the time range of 500–4000 h show a strong linear fit to equation (1), with an R^2 value of 0.96 and a slope 5.9×10^{-10} m/s$^{1/2}$. The experimentally determined value of k can then be compared with theoretical values of k to determine how well the models explain the data.

Calculations of k in various models use slightly different methods based on the assumptions and concentration gradients used. The model most applicable to the work here is the one proposed by Maldonado and Nembach for a PFZ in a Ni-based superalloy [28]. While they concluded that the PFZ was due to the depletion of Ti, which led to the dissolution of γ' precipitates, this same model can be applied to Fe–20Cr–30Ni–2Nb–5Al due to the depletion of Ni. This model can be represented by the concentration gradient in Fig. 13.

Using the following assumptions: 1) $GB\_w/2$ is much smaller than w, and 2) the volume diffusion coefficient (D) and concentration gradient within the PFZ are constant, yields the following equation [28]:

$$k = \left[2D\frac{C_{PFZ/m} - C_{GB/PFZ}}{C_m - C_{PFZ/m}}\right]^{1/2} \qquad \text{equation 2}$$

Where D is the volume diffusion coefficient of Ni in austenite, which is estimated from the literature [46] to be 3.9×10^{-19} m [2]/s at 750 °C, and the concentration for each location is estimated from EDS line scans as presented in Fig. 10, using values of $C_m = 0.31$, $C_{PFZ/m} = 0.29$, and $C_{GB/PFZ} = 0.275$. Inserting these values into the model gives a theoretical value of $k = 7.6 \times 10^{-10}$ m/s$^{1/2}$. The experimentally derived value of k

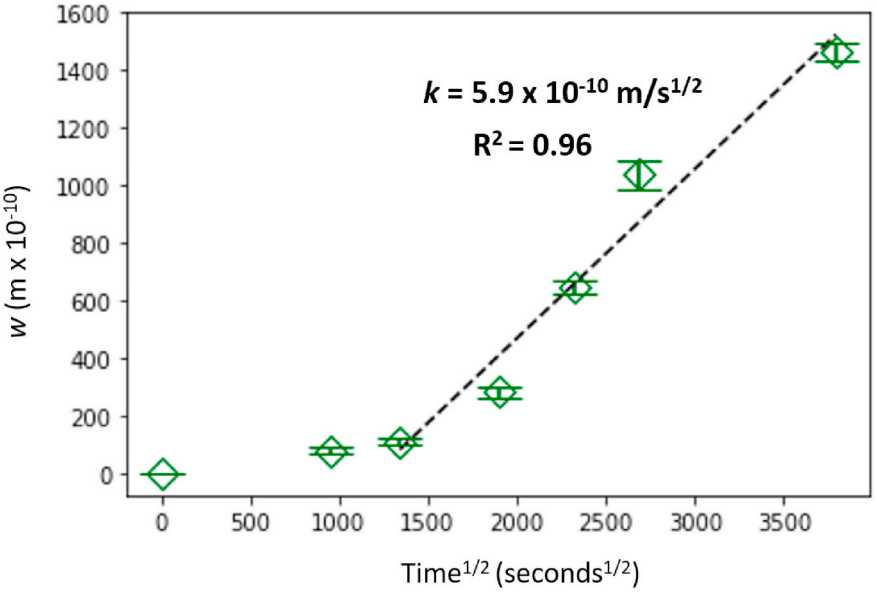

Fig. 12. PFZ width w versus square-root of time for Fe–20Cr–30Ni–2Nb–5Al at 750 °C. As the head and gauge showed little difference in width, the measurements were combined for each creep time. The error bars represent 95% confidence intervals.

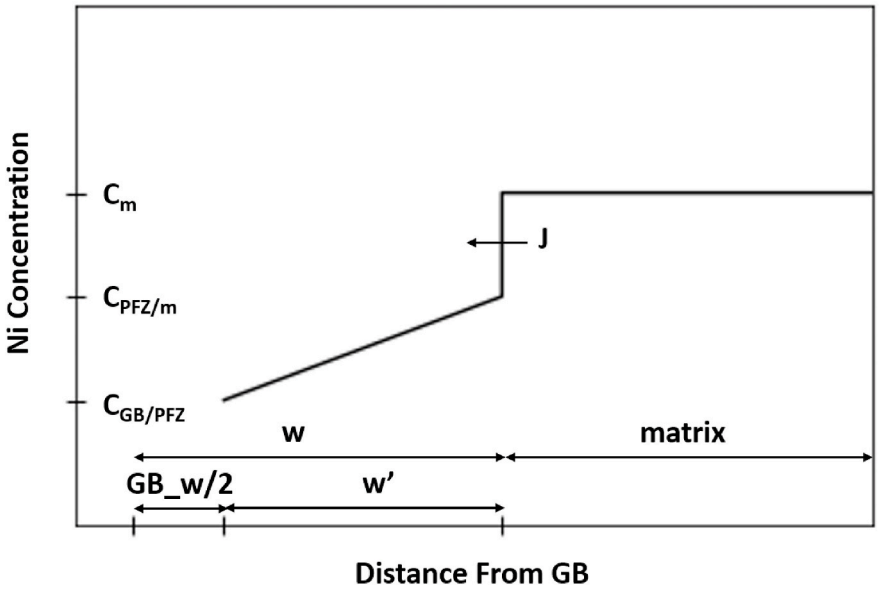

Fig. 13. *Concentration gradient for PFZ growth model proposed by Maldonado and Nembach [28] applied to Fe–20Cr–30Ni–2Nb–5Al using Ni as the depleted element. J represents the flux of Ni atoms.*

$= 5.9 \times 10^{-10}$ m/s$^{1/2}$ shows good agreement with this theoretical value. The calculation of the experimental and theoretical values of k assumes that k remains constant throughout creep. While this is likely not completely true as the concentration gradient in the PFZ may change with creep time, this is a reasonable assumption for the time period of 500 h–4000 h where w shows a strong linear fit with $t^{1/2}$. While the mechanism of growth in Fe–20Cr–30Ni–2Nb–5Al is more complicated than the model suggests – as both direct and indirect solute loss are possibly occurring in this alloy – the relatively good agreement with this simple model helps to confirm that the growth of the PFZ is due to diffusion through the matrix.

These results of little PFZ growth initially followed by significant PFZ growth at longer times are somewhat similar to the results of a study on a Al–Cu–Mg–Mn alloy, in which the researchers reported three stages [35]. Stage one, where a PFZ first formed due to vacancy depletion; stage two where the PFZ disappeared or was very small; and stage three, a period of substantial PFZ growth due to solute depletion. In the present study, no stage one was observed. It is possible; however, that stage one occurred but that no creep tests of sufficiently short length were performed to observe it.

Further, a plot of w' vs GB precipitate width shows a very good linear fit, see Fig. 14, indicating that as the GB precipitates grow and consume more solute, the width of the PFZ increases. It should be noted that this plot not only contains the data at 750 °C, but also the data at 730 °C and 770 °C. This indicates that the PFZ width may be controlled by the width of the GB precipitates. This further confirms that PFZ growth is due to solute depletion, because as the GB precipitates coarsen they will further deplete the surrounding grain of Ni. This also suggests that stabilizing GB precipitates at smaller sizes could reduce the width of the PFZ.

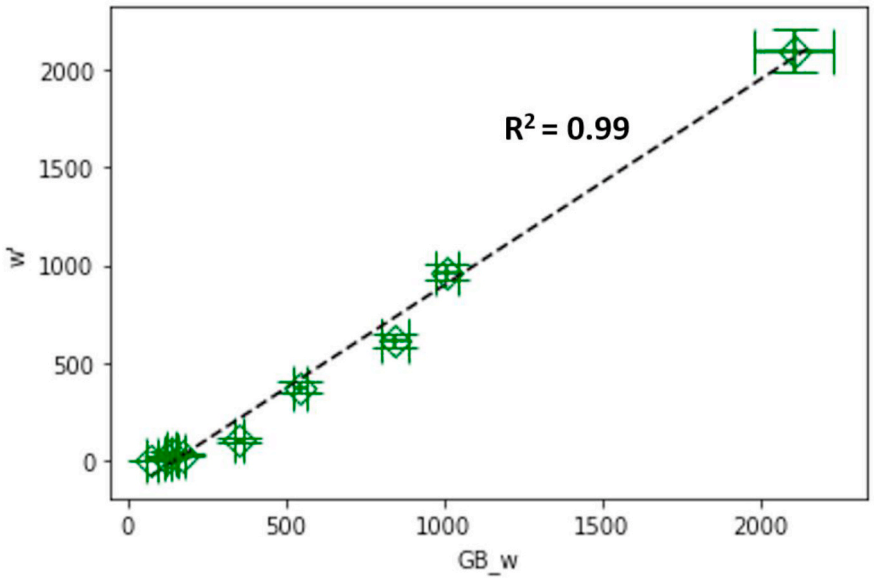

Fig. 14. GB_w vs PFZ width w' for Fe–20Cr–30Ni–2Nb–5Al at temperatures of 730 °C, 750 °C, and 770 °C for various times. As the head and gauge showed little difference in width, the measurements were combined for each creep time. The error bars represent 95% confidence intervals.

4.3. Effect on mechanical properties

Prior research on Fe–20Cr–30Ni–2Nb–5Al showed that $L1_2$ precipitates were the dominant strengthening mechanism in the matrix [11]. Thus, it is reasonable to assume that the PFZ will be weaker than the $L1_2$-strengthened matrix. This is supported by work introduced in the introduction on other alloys, which showed that the PFZ is softer than the surrounding precipitation-hardened matrix and leads to a decrease in yield strength [27,37–40]. Previous studies have shown that Fe–20Cr–30Ni–2Nb–5Al exhibits an intergranular fracture surface after high temperature tests performed to failure [11,12,16]. In this study, micro-cracks were observed in the PFZ after creep at 750 °C and 45 MPa for 4000 h (stopped prior to failure). These micro-cracks suggest that failure of this alloy initiates in the PFZ – and that failure likely occurs when these micro-cracks are able to propagate along the PFZ and ultimately result in the intergranular failure. These micro-cracks, along with the intergranular frature mode, suggest that the PFZ ultimately compromises the high temperature strength of the alloy.

5. Conclusions

- A $L1_2$ (Ni_3Al) PFZ forms along the GBs and around Laves phase and B2 precipitates in the matrix due to Ni and Al depletion.
- This solute depletion is due to direct loss of Ni and Al to B2 NiAl precipitates, as well as an indirect loss of Ni and Al due to local composition changes near Laves phase precipitates and GBs.
- The growth of the PFZ is modeled well by diffusion of Ni through the matrix. Little growth occurs initially when the GB precipitates are small and cover less then ~60% of the GB. When the GB precipitates increase in width and GB coverage, sufficient solute is consumed by the GB precipitates to dissolve the $L1_2$ precipitates and. thus, the growth rate increases.
- The width of the PFZ shows a strong linear relationship with GB precipitate width. This further supports a mechanism involving PFZ formation and growth due solute depletion, as the increased size of the GB precipitates will further deplete the surrounding area of solute.
- Micro-cracks observed in the PFZ when the test was stopped prior to failure indicate that the PFZ is weaker than the $L1_2$ containing matrix, and that fracture likely initiates in the PFZ.

Data availability

The raw/processed data required to reproduce these findings is available at https://data.mendeley.com/datasets/gdztxr4y6f/1.

CRediT authorship contribution statement

Andrew Peterson: Conceptualization, Methodology, Investigation, Writing – original draft, Visualization, Formal analysis. **Ian Baker:** Conceptualization, Resources, Writing – Editing and Review, Funding acquisition.

Declaration of competing interest

The authors declare that they have no known competing financial interests or personal relationships that could have appeared to influence the work reported in this paper.

Acknowledgements

This research was supported by National Science Foundation (NSF) Grant DMR 1708091. Any opinions, findings, and conclusions or recommendations expressed in this material are those of the author(s) and do not necessarily reflect the views of the NSF. Michael Schmidt of Carpenter Technology Corporation (Wyomissing, PA) provided the ingots. The use of the Dartmouth Electron Microscope Facility is gratefully acknowledged.

References

[1] R. Viswanathan, W. Bakker, Materials for ultrasupercritical coal power plants - boiler materials: Part 1, J. Mater. Eng. Perform. 10 (1) (2001) 81–95, https://doi.org/10.1361/105994901770345394.
[2] R. Viswanathan, J.F. Henry, J. Tanzosh, et al., U.S. Program on materials Technology for ultra-supercritical coal power plants, J. Mater. Eng. Perform. 14 (3) (2005) 281–292, https://doi.org/10.1361/10599490524039.
[3] J.P. Shingledecker, I.G. Wright, Evaluation of the Materials Technology Required for a 760?C Power Steam Boiler, 2006. Published online January 1, https://www.osti.gov/biblio/931631.
[4] M.P. Brady, Y. Yamamoto, M.L. Santella, et al., The development of alumina-forming austenitic stainless steels for high-temperature structural use, JOM (J. Occup. Med.) 60 (7) (2008) 12–18, https://doi.org/10.1007/s11837-008-0083-2.
[5] Y. Yamamoto, M.P. Brady, M.L. Santella, H. Bei, P.J. Maziasz, B.A. Pint, Overview of strategies for high-temperature creep and oxidation resistance of alumina-forming austenitic stainless steels, Metall. Mater. Trans. 42 (4) (2011) 922–931, https://doi.org/10.1007/s11661-010-0295-2.
[6] M.P. Brady, J. Magee, Y. Yamamoto, D. Helmick, L. Wang, Co-optimization of wrought alumina-forming austenitic stainless steel composition ranges for high-temperature creep and oxidation/corrosion resistance, Mater. Sci. Eng., A 590 (2014) 101–115, https://doi.org/10.1016/J.MSEA.2013.10.014.
[7] M.P. Brady, Y. Yamamoto, M.L. Santella, L.R. Walker, Composition, microstructure, and water vapor effects on internal/external oxidation of alumina-forming austenitic stainless steels, Oxid Met 72 (5–6) (2009) 311–333, https://doi.org/10.1007/s11085-009-9161-2.
[8] M.P. Brady, K.A. Unocic, M.J. Lance, M.L. Santella, Y. Yamamoto, L.R. Walker, Increasing the upper temperature oxidation limit of alumina forming austenitic stainless steels in air with water vapor, Oxid Met 75 (5–6) (2011) 337–357, https://doi.org/10.1007/s11085-011-9237-7.
[9] X. Xu, X. Zhang, G. Chen, Z. Lu, Improvement of high-temperature oxidation resistance and strength in alumina-forming austenitic stainless steels, Mater. Lett. 65 (21–22) (2011) 3285–3288, https://doi.org/10.1016/j.matlet.2011.07.021.
[10] Y. Yamamoto, G. Muralidharan, M.P. Brady, Development of L12-ordered Ni3(Al, Ti)-strengthened alumina-forming austenitic stainless steel alloys, Scripta Mater. 69 (11–12) (2013) 816–819, https://doi.org/10.1016/J.SCRIPTAMAT.2013.09.005.
[11] A. Peterson, I. Baker, Microstructural evolution of Fe-20Cr-30Ni-2Nb-5Al AFA Steel during creep at 760°C, *Mater Sci Eng A*. Published online November 29 (2020) 140602, https://doi.org/10.1016/j.msea.2020.140602.
[12] I. Baker, N. Afonina, Z. Wang, M. Wu, Preliminary creep testing of the alumina-forming austenitic stainless steel Fe-20Cr-30Ni-2Nb-5Al, Mater. Sci. Eng., A 718 (2018) 492–498, https://doi.org/10.1016/J.MSEA.2018.01.090.
[13] B. Hu, I. Baker, The effect of thermo-mechanical treatment on the high temperature tensile behavior of an alumina-forming austenitic steel, Mater. Sci. Eng., A (2016), https://doi.org/10.1016/j.msea.2015.11.036. Published online.
[14] B. Hu, G. Trotter, Z. Wang, S. Chen, Z. Cai, I. Baker, Effect of Boron and Carbon Addition on Microstructure and Mechanical Properties of the Aged Gamma-Prime Strengthened Alumina-Forming Austenitic Alloys, 2017, https://doi.org/10.1016/j.intermet.2017.06.011. Intermetallics. Published online.
[15] B. Zhao, J. Fan, Y. Liu, et al., Formation of L12-ordered precipitation in an alumina-forming austenitic stainless steel via Cu addition and its contribution to creep/rupture resistance, Scripta Mater. 109 (2015) 64–67, https://doi.org/10.1016/j.scriptamat.2015.07.019.
[16] A. Peterson, I. Baker, Analysis of the elevated temperature deformation mechanisms and grain boundary strengthening of the alumina-forming austenitic stainless steel Fe-20Cr-30Ni-2Nb-5Al, Mater. Sci. Eng., A (2021) 141219, https://doi.org/10.1016/j.msea.2021.141219. Published online April 8.
[17] I. Tarigan, K. Kurata, N. Takata, T. Matsuo, M. Takeyama, Novel concept of creep strengthening mechanism using grain boundary Fe $_2$ Nb Laves phase in austenitic heat resistant steel, MRS Proc 1295 (2011), https://doi.org/10.1557/opl.2011.558 mrsf10-1295-n06-03.
[18] H. Wen, B. Zhao, X. Dong, F. Sun, L. Zhang, A systematic investigation of precipitates in matrix and at grain boundaries in an alumina-forming austenitic steel during creep testing at 700 °C, Metall Mater Trans A Phys Metall Mater Sci 51 (8) (2020) 4186–4194, https://doi.org/10.1007/s11661-020-05848-4.
[19] J.P. Poirier, Creep of crystals: high-temperature deformation processes in metals, ceramics, and minerals, Cambridge University Press, 1985.
[20] T.B. Gibbons, The influence of diffusion creep on precipitate-free zone formation in ni-20% cr-base alloys, Sci. J. 6 (1) (1972) 13–16, https://doi.org/10.1179/030634572790446172.
[21] J. Wadsworth, O.A. Ruano, O.D. Sherby, Denuded zones, diffusional creep, and grain boundary sliding, Metall Mater Trans A Phys Metall Mater Sci 33 (2) (2002) 219–229, https://doi.org/10.1007/s11661-002-0084-7.
[22] J. Wolfenstine, O.A. Ruano, J. Wadsworth, O.D. Sherby, Refutation of the relationship between denuded zones and diffusional creep, Scripta Metall. Mater. 29 (4) (1993) 515–520, https://doi.org/10.1016/0956-716X(93)90157-N.
[23] P.N.T. Unwin, G.W. Lorimer, R.B. Nicholson, The origin of the grain boundary precipitate free zone, Acta Metall. 17 (11) (1969) 1363–1377, https://doi.org/10.1016/0001-6160(69)90154-0.

[24] C.R. Shastry, G. Judd, A study of grain boundary precipitate-free zone formation in an Al-Zn-Mg alloy, *Metall Mater Trans B*. Published online (1971), https://doi.org/10.1007/BF02811608.
[25] H.S. Rosenbaum, D. Turnbull, Metallographic investigation of precipitation of silicon from aluminum, Acta Metall. 7 (10) (1959) 664–674, https://doi.org/10.1016/0001-6160(59)90143-9.
[26] H.S. Rosenbaum, D. Turnbull, On the precipitation of silicon out of a supersaturated aluminum-silicon solid solution, Acta Metall. 6 (10) (1958) 653–659, https://doi.org/10.1016/0001-6160(58)90160-3.
[27] T. Krol, D. Baither, E. Nembach, The formation of precipitate free zones along grain boundaries in a superalloy and the ensuing effects on its plastic deformation, Acta Mater. 52 (7) (2004) 2095–2108, https://doi.org/10.1016/j.actamat.2004.01.011.
[28] R. Maldonado, E. Nembach, The formation of precipitate free zones and the growth of grain boundary carbides in the nickel-base superalloy NIMONIC PE16, Acta Mater. 45 (1) (1997) 213–224, https://doi.org/10.1016/S1359-6454(96)00139-5.
[29] A. Partridge, F.W. Noble, G.J. Tatlock, The effects of long-term ageing on Nimonic PE16, J. Nucl. Mater. 186 (2) (1992) 100–116, https://doi.org/10.1016/0022-3115(92)90327-H.
[30] D.P. Yao, Y.Z. Zhang, Z.Q. Hu, Y.Y. Li, C.X. Shi, The formation and growth of PFZ at grain boundary in Al-11.9at.-%Li alloy, Scripta Metall. 23 (4) (1989) 537–541, https://doi.org/10.1016/0036-9748(89)90447-X.
[31] K.B. Rao, V. Seetharaman, S.L. Mannan, P. Rodriguez, Precipitation, deformation and fracture behaviour of a thermomechanically processed nimonic PE 16 superalloy, J. Nucl. Mater. 102 (1–2) (1981) 7–16, https://doi.org/10.1016/0022-3115(81)90540-7.
[32] S.C. Jha, T.H. Sanders, M.A. Dayananda, Grain boundary precipitate free zones in Al-Li alloys, Acta Metall. 35 (2) (1987) 473–482, https://doi.org/10.1016/0001-6160(87)90253-7.
[33] H. Rösner, K. Neuking, M. Kolbe, E. Nembach, Precipitate-free zones at the grain boundary of a bicrystal of the nickel-base superalloy nimonic PE16, Mater. Sci. Forum (1993). https://doi.org/10.4028/www.scientific.net/msf.126-128.443. Published online.
[34] Tien JK, Gamble RP. The Influence of Applied Stress and Stress Sense on Grain Boundary Precipitate Morphology in a Nickel-Base Superalloy during Creep. Vol vol. 2.; 1971. doi:10.1007/BF02913891.
[35] Y.Q. Chen, S.P. Pan, S.W. Tang, W.H. Liu, C.P. Tang, F.Y. Xu, Formation mechanisms and evolution of precipitate-free zones at grain boundaries in an Al–Cu–Mg–Mn alloy during homogenisation, J. Mater. Sci. 51 (16) (2016) 7780–7792, https://doi.org/10.1007/s10853-016-0062-x.
[36] T.D. Nguyen, K. Sawada, H. Kushima, M. Tabuchi, K. Kimura, Change of precipitate free zone during long-term creep in 2.25Cr-1Mo steel, Mater. Sci. Eng., A (2014), https://doi.org/10.1016/j.msea.2013.10.101. Published online.
[37] T. Ogura, S. Hirosawa, T. Sato, Science and Technology of Advanced Materials Quantitative Characterization of Precipitate Free Zones in Al-Zn-Mg(-Ag) Alloys by Microchemical Analysis and Nanoindentation Measurement Quantitative Characterization of Precipitate Free Zones in Al-Zn-Mg(-Ag), 2004, https://doi.org/10.1016/j.stam.2004.02.007. Published online.
[38] V. Radmilovic, C. Taylor, Z. Lee, A. Tolley, D. Mitlin, U. Dahmen, Nanoindentation properties and the microstructure of grain boundary precipitate-free zones (PFZs) in an AlCuSiGe alloy, Philos. Mag. A 87 (26) (2007) 3905–3919, https://doi.org/10.1080/14786430601153414.
[39] D. Baither, T. Krol, E. Nembach, *In-situ* transmission electron microscopy study of dislocation processes at precipitate-free zones in a γ' -strengthened superalloy, Philos. Mag. A 83 (35) (2003) 4011–4029, https://doi.org/10.1080/14786430310001603445.
[40] T. Krol, D. Baither, E. Nembach, Quantification of the detrimental effects of precipitate free zones on the yield strength of a superalloy, Scripta Mater. 48 (8) (2003) 1189–1194, https://doi.org/10.1016/S1359-6462(02)00566-3.
[41] F. Garofalo, O. Richmond, W.F. Domis, Design of apparatus for constant-stress or constant-load creep tests, J Fluids Eng Trans ASME 84 (2) (1962) 287–293, https://doi.org/10.1115/1.3657303.
[42] G. Trotter, I. Baker, The effect of aging on the microstructure and mechanical behavior of the alumina-forming austenitic stainless steel Fe–20Cr–30Ni–2Nb–5Al, Mater. Sci. Eng., A 627 (627) (2015) 270–276, https://doi.org/10.1016/j.msea.2014.12.072.
[43] B. Hu, I. Baker, M.S.J. Kernion, M.P. Brady, Y. Yamamoto, Creep failure OF the alumina-forming austenitic stainless steel dafa 29, in: Advances in Materials Technology for Fossil Peower Plants_Proceedings from the Eight International Conference, 2016, pp. 295–303.
[44] L.S. Muratov, B.R. Cooper, Segregation of niobium solute in nickel toward grain boundaries and free surfaces, J. Phase Equil. 19 (6) (1998) 503–512, https://doi.org/10.1361/105497198770341671.
[45] M. Gao, R.P. Wei, Grain boundary γ'' precipitation and niobium segregation in inconel 718, Scripta Metall. Mater. 32 (7) (1995) 987–990, https://doi.org/10.1016/0956-716X(95)00062-Z.
[46] H.K.D.H. Bhadeshia, S.R. Honeycombe, Iron and its interstitial solid solutions, in: Steels, Elsevier, 2006, pp. 1–16, https://doi.org/10.1016/b978-075068084-4/50003-0.